Nuclear Materials and Energy 12 (2017) 253–260

Contents lists available at ScienceDirect

Nuclear Materials and Energy

journal homepage: www.elsevier.com/locate/nme

ERO modelling of tungsten erosion in the linear plasma device PSI-2

A. Eksaeva[a,b,*], E. Marenkov[a], D. Borodin[b], A. Kreter[b], M. Reinhart[b], A. Kirschner[b], J. Romazanov[b], A. Terra[b], S. Brezinsek[b], K. Nordlund[a,c]

[a] National Research Nuclear University MEPhI, 31, Kashirskoe sh., 115409, Moscow, Russia
[b] Forschungszentrum Jülich GmbH, Institut für Energie- und Klimaforschung - Plasmaphysik, Partner of the Trilateral Euregio Cluster (TEC), 52425 Jülich, Germany
[c] Department of Physics, University of Helsinki, FI-00560 Helsinki, Finland

ARTICLE INFO

Article history:
Received 15 July 2016
Revised 27 January 2017
Accepted 9 March 2017
Available online 23 March 2017

ABSTRACT

Series of experiments on tungsten (W) erosion and transport in Argon (Ar) plasma were conducted at the linear plasma device PSI-2. W erosion was measured with three independent methods: WI spectroscopy, mass loss and quartz micro-balance (QMB) deposition sensor. Consistent set of data produced in these experiments was interpreted using the 3D ERO code simulations, which have reproduced all the main trends observed. Influence of the physical model assumptions (e.g. energy and angular distributions of sputtered particles) was demonstrated. The effect of WI effective quasi-metastable (MS) state population dynamics on spectroscopy measurements is shown; the characteristic relaxation time is determined. The measured physical sputtering yields for W are close to the simulated data obtained in the binary collision approximation (BCA) approach (SDTrimSP code). The remaining discrepancies between simulations and the experiment, mostly in spectroscopy, are accounted to the uncertainties in the plasma parameters and atomic data.

1. Introduction

Plasma-surface interaction (PSI) determines the duty cycle of ITER to a large extent. Physical erosion limits the lifetime of plasma-facing components (PFC) and influences the retention of tritium due to the co-deposition. Tungsten (W) is of particular interest because it was chosen as the main material for the divertor area of ITER due to its high melting temperatures, low sputtering yield and low tritium retention [1]. Linear devices such as PISCES-B [2], PILOT-PSI [3] and PSI-2 [4,5] have a number of advantages for investigating specific problems of PSI [6]: continuous operation, compactness, straightforward geometry and facilitated control over the experimental parameters. Plasma parameters in these devices can be relevant to boundary and divertor areas of tokamaks.

Numerical simulations are the key for understanding of all variety of PSI processes in the experiment and their resulting interplay. 3D local impurity transport and PSI code ERO is an established tool for predictive modelling of ITER issues [7]. It has already been applied for modelling of experiments at linear plasma devices including PISCES-B [8], Pilot-PSI [9] and PSI-2 [10].

Several experiments dedicated for ERO and underlying erosion data benchmark were carried out recently at PSI-2 in which the physical sputtering of the W target by Ar plasma was characterized by passive optical emission spectroscopy, weight loss with spatial resolution and quartz micro balance (QMB) deposition sensor measurements serving as a movable witness plate. In combination these measurements are capable of giving a full picture of erosion and transport processes in linear plasmas, including relation between the net erosion, determined by QMB and weight loss, and the gross erosion, determined by spectroscopy. The energy of the sputtering Ar ions E_{in} was scanned at various plasma conditions by applying the additional negative target biasing.

The focus of this work is ERO application for the interpretation of the PSI-2 experiments mentioned. A detailed comparison of numerical modelling results with the experiment provides an opportunity to study the particular effects and estimate uncertainties. The angular and energy distributions of sputtered particles in a parametric form were introduced into the code and shown to be essential for reproducing the spectroscopy results. An essential role of the introduced effective quasi-metastable states (MS) population dynamics for spectroscopy measurements is shown and their characteristic relaxation time is fitted by matching of ERO simulations with the experiment. Physical erosion yields were determined from the experiment using the ERO-based interpretation which allows

* Corresponding author.
E-mail address: a.eksaeva@fz-juelich.de (A. Eksaeva).

http://dx.doi.org/10.1016/j.nme.2017.03.014

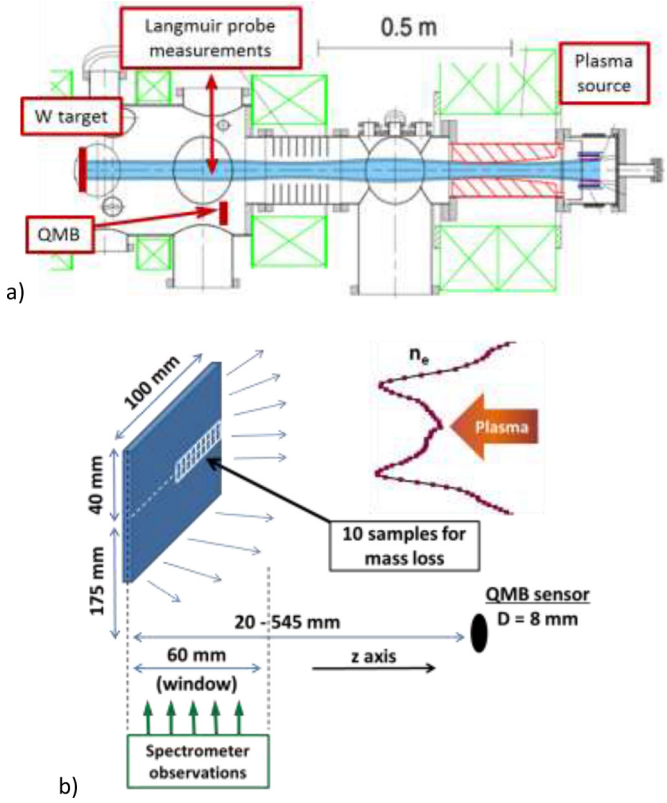

Fig. 1. Scheme of the experimental set up on PSI-2: a) scheme of the installation with main diagnostics marked; b) scheme of the experiment with marked distances.

taking into account, i.e. substrate, the role of the W redeposition including prompt effects. The resulting yields were compared with the data based on the SDTrimSP code calculations (in the binary collision approximation (BCA)) expressed in the form of an approximation formula [11,33] taking into the account the dependence on E_{in}.

The paper is organized as follows. In Section 2 the PSI-2 experiments are described; Section 3 is dedicated to the ERO code description; in Section 4 modelling results are presented together with discussion of the underlying data and taken assumptions.

2. W erosion experiments at PSI-2

The linear plasma device PSI-2 [4] produces a plasma column confined by an axial magnetic field. Absolute value of the magnetic field B changes significantly along the main axis; however it can be easily determined from the known coils configuration and electrical current in those. A typical B field value in the target exposure region is 0.1 T.

In these particular experiments, which were dedicated to erosion data and model benchmark, the W target was irradiated with Ar plasma ($T_e \approx 2-4$eV, $n_e \approx 10^{12}$cm^{-3}). Later, to avoid uncertainties due to recombination and low temperature of Ar plasma, similar experiments were also performed in Ne plasma - weight loss measurements are presented later in the paper. Detailed information on the experiments can be found in [12].

The experiment setup is given in Fig. 1. Radial profiles of electron density and temperature were measured by means of a reciprocating Langmuir probe which was positioned 310 mm from the target surface along the installation axis [4]. One can see in Fig. 2 that both n_e and T_e profiles have clear minima at the plasma column centre. Such hollow plasma configuration is typical for PSI-2 due to the cylindrical cathode in the plasma source [4]. The

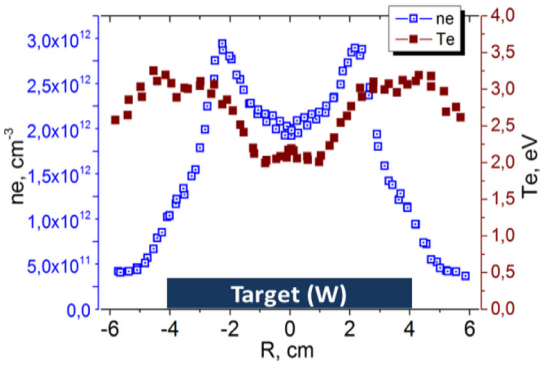

Fig. 2. Radial distribution of Ar plasma parameters (T_e, n_e) in PSI-2 facility, "high" discharge power.

rectangular 80×100 mm^2 W target was positioned at the installation axis perpendicularly to the magnetic field lines. The target was under negative bias voltage U_b whish was varying from -50 V to -150 V, controlling incident ions energies. Together with negative plasma potential $U_p \approx -10$ V this bias resulted in incident ions energies $E_{in} \approx 40$–140 eV. Ten 5×5 mm^2 polished W samples were imbedded into the target for weight loss measurements and post-mortem analyses.

Three independent measurement techniques were used in these experiments:

(a) spectroscopy profiles in two orthogonal directions providing the 2D emission intensity pattern and axial intensity profiles near the target surface;
(b) QMB in situ deposition sensor serving as a witness plate with a varying axial position with respect to the target;
(c) weight loss with spatial resolution;

However, for instance, the exposure for mass loss measurement cannot be combined with the target bias voltage scan affecting the erosion rate. It is also unreasonable to change the biasing and witness plate position (QMB) at the same time. The measurements and parameter scans performed during the experiments are summarized in the Table 1 for three plasma conditions characterised by the discharge power, determined by the arc discharge current in the plasma source $I_{disch} = 50$ A, *100* A, *150* A, referred later to as 'low', 'medium' and 'high' power, respectively.

The main difference between discharge power cases is the n_e absolute value determining the ionization, local transport and spectroscopy of eroded W. There is also a much higher concentration of Ar^{2+} ions in "high" discharge plasma than in "low" one. Ar^{2+} concentration variations have already been detected in previous experiments at PSI-2 [13] with the in-situ mass-spectrometer of magnetized plasmas (see Table 2).

WI ($\lambda = 400.9$ nm) light emission intensity profiles along the installation axis $I_{WI}(z)$ (see Fig. 3) and perpendicularly to it $I_{WI}(r)$ in a 60 mm area from the surface were measured by the spectrometer for various discharge power cases and U_b values. The set of radial intensity profiles taken every 5 mm from the target surface $I_{WI}(r)$ allows reconstructing the 2D emission intensity pattern (side view integrated along the line of sight from the vessel window perpendicular to the device axis (Fig. 1)); axial intensity profiles $I_{WI}(z)$ can contribute analysing the impurities penetration in plasma.

QMB deposition sensor was initially positioned at 345 mm from the target in axial direction. Later on the scan of the axial target position was performed ($R_{QMB}(L)$, L = 20 ÷ 545 mm) in order to analyse angular patterns of the sputtered particles. The radial position of QMB was constantly 175 mm. The QMB signal as a function of the target bias voltage $R_{QMB}(U_b)$ was measured for various pa-

Table 1
W erosion experiments at the PSI-2 facility [12].

#	Plasma	Discharge power	E_{in}	n_e	T_e	What was measured
1	Ar	"Low" "Medium" "High"	40–140 eV step: 10 eV	≈ 0.4–2.5 x 10^{12} cm^{-3}	≈ 2–4 eV	For each U_b and each plasma power value: • $I_{WI}(z)$ - WI line emission intensity profile along the z axis (λ = 4009 Å); • $R_{QMB}(U_b)$ - QMB sensor signal value;
2	Ar	"High" (long irradiation)	≈ 140 eV	≈ 2.0–2.5 x 10^{12} cm^{-3}	≈ 3.5 eV	• 2D line emission patterns; • M_{lost}(r) - weight loss;
3	Ar	"Low" (long irradiation)	≈ 140 eV	≈ 0.4–0.5 x 10^{12} cm^{-3}	≈ 3.0 eV	• 2D line emission patterns; • $R_{QMB}(L)$ - QMB signal vs. distance between the target and the QMB; • M_{lost}(r) - weight loss;
4	Ne	"High" "Low" (long irradiation)	≈ 140 eV	≈ 0.1–1.4 x 10^{12} cm^{-3}	≈ 4–10 eV	• M_{lost}(r) - weight loss;

Table 2
Ar^{2+} relative concentration measurements at PSI-2 at the radial plasma density maximum [13].

I_{disch}, A	Ar^{2+}/Ar^{+}
50	0,015
100	0,14
150	0,39

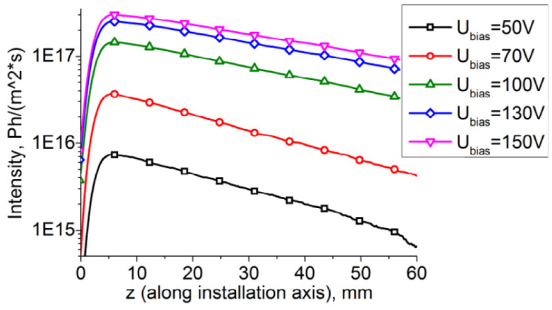

Fig. 3. Axial WI (λ = 400.9 nm) intensity profiles – Ar experiment. "High" discharge power, U_b = 50–150 V, experiment 1 (see Table 1).

rameter cases to understand the influence of the discharge power on the sputtering intensity.

3. ERO modelling

The 3D Monte-Carlo (MC) code ERO [14] is a tool for numerical simulation of impurity transport in plasma, PSI processes and the interpretation of experiments, e.g. it can simulate the spectroscopic patterns and the PFC surface composition. It is based on the test particle approximation: impurity species are tracked in a given background plasma, which is not influenced by the impurities. The background plasma parameters at each location (n_e, T_e, B, etc.) are taken as an input. It is possible to use simulated plasma backgrounds like for ITER [7]; however in the present work the experimental data were used. The initial parameters for the test particles, e.g. velocities and movement directions, are generated randomly with appropriate distributions. The elementary processes (e.g. ionization, recombination, elastic collisions with plasma particles, etc.) are also treated in the MC way. Test particles trajectories are calculated using the Boris method [15] taking into account 3D electromagnetic fields, perpendicular diffusion and plasma friction.

ERO utilizes Cartesian coordinates; for linear devices z axis is assumed to coincide with the installation axis. All simulated volume is divided into 3D rectangular space cells. Tracking of impurity particles allows calculating their density in any simulation volume cell and then to estimate corresponding light emission using photon emission coefficients – PEC [16] dependent on the local plasma parameters. Impurity particles start from the target surface as neutrals. Their amount, i.e. erosion rate, is calculated by the approximation formulas proposed by Eckstein [11]. The fits are based on SDTrimSP code (BCA) simulations.

Computer code ERO has already been applied for modelling of experiments at linear plasma devices (e.g. PISCES-B [8]). However, in order to use it for numerical simulation of the PSI-2 experiments some new features were implemented including the exact geometry of the target and observation system, experimental plasma parameters (n_e, T_e) and electromagnetic field configuration. The synthetic diagnostic features like the spectroscopy integration along the user-defined line of sight and the geometrical configuration of the QMB deposition sensor were provided.

Physical model modifications included a possibility to set different energy and angular distributions of sputtered particles as a function of incident ions energies. Another incorporated effect is the alterations of the Ar^{2+} concentration with respect to the plasma discharge power, based on the data from [13]. The E_{in} doubles for Ar^{2+}, which is critical for the sputtering rate. Metastable (MS) tracking introduced earlier in ERO [8] for BeI was adapted for the WI emission in this work, including matching the effective relaxation time from the experiment.

Plasma density variations in axial direction were calculated according to the P.C. Stangeby 1D flow model [17]. It was shown experimentally that this model is the best approximation of Mach number axial profile in the PISCES-B linear plasma facility [18]; the same was observed about n_e axial profile in PISCES-B [19]. The same model is used in other ERO simulations for linear devices e.g. [37]. According to this model n_e value decreases towards the target:

$$n_e(z) = n_e \frac{L_{conn} - z}{2L_{conn}\left(\frac{L_{conn}}{L_{conn}-z} - \sqrt{\left(\frac{L_{conn}}{L_{conn}-z}\right)^2 - 1}\right)} \quad (1)$$

where z is the distance from the target surface, $z < L_{conn}$, L_{conn} – connection length symbolizing the distance where the n_e starts to decrease, n_e – plasma density value according to the Langmuir probe (assuming its position $z_{probe} > L_{conn}$). The connection length at PSI-2 was estimated by measuring plasma parameters profiles

for different positions of the target with respect to the Langmuir probe (the target plays role of a neutralizer plate in this case since it covers all plasma column). During these measurements the connection length was estimated as L = 1000 mm. We assume that due to the measurement method the uncertainty can be large in this case. However, in the same time, ERO sensitivity scans have shown that increasing/decreasing this length by 200–300 mm should not change the final result significantly. Parallel electric field is calculated through the n_e gradient. An additional sheath electric field caused by the voltage drop near the biased target is taken into account.

4. Results and discussion

The significant uncertainties in the simulations of the experiment are energy and angular distributions of sputtered particles. Strong influence of these factors is shown and discussed in our previous work [10]. For low energies of incident ions ($E_{in} = 40 \div 140$eV) both energy and angular distributions have quite specific shapes (in comparison with high energy cases) which are sensitive for variations of E_{in}. Ionization and recombination cross-section values used in the code also bring a notable uncertainty, because for the temperature interval of $T_e = 2$–4 eV the data from different sources scatters significantly. Finally accounting for WI metastables plays a significant role in reproducing the shape of the axial WI line emission intensity profile.

By varying these parameters within reasonable ranges one can understand their influence on the final result and find a set of parameters giving the best agreement with all experimental data simultaneously. The extensive data set and independence of measurements techniques make this choice of parameters quite unique and unambiguous.

There are overall 6 experimental relations observed in the PSI-2 experiments which are useful for benchmarking of the ERO modelling (Table 1):

- $M_{lost}(r)$ - radially resolved weight loss measurements for “low” and “high” discharge power.
- $R_{QMB}(L)$ - dependence of QMB signal on the distance between the target and the sensor;
- $R_{QMB}(U_b)$ - dependence of QMB signal on the bias voltage U_b applied to the target for different discharge power values;
- $I_{WI}(z)$ – axial WI line intensity ($\lambda = 400.9$ nm) profiles at various conditions;
- $I_{WI}(r)$ – vertical (orthogonal to axis) profiles of WI line emission intensity at different distances from the target surface (2D sputtering patterns can be reconstructed);

Below we consider in detail ERO simulations aimed to reproduce each of these relations. We are paying a particular attention to the assumptions made, related uncertainties in the underlying data and free parameters of the model.

4.1. Angular distribution of sputtered particles

For low incident ion energies the angular distribution of sputtered particles has a characteristic shape in the polar coordinates called “butterfly-like” (Fig. 4), acquiring maximum sputtering at a certain angle from surface [20,22]. Angular distributions of sputtered atoms in this case can be expressed with an approximation formula [21]:

$$f(\theta) = A\cos^n(\theta) - B\cos^m(\theta) \quad (2)$$

Here A, B, m, n – coefficients, different for various materials and influenced by irradiation parameters; It is known from the

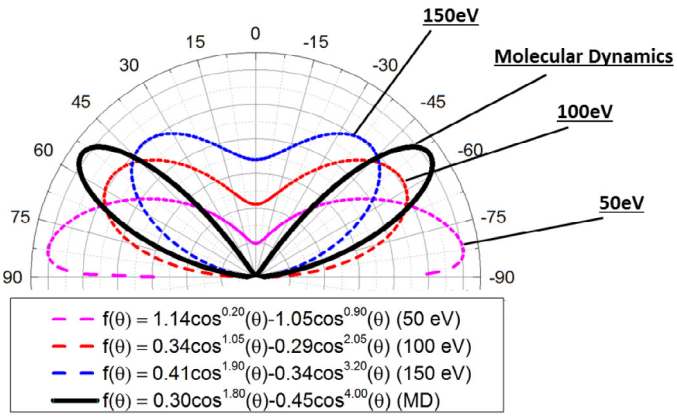

Fig. 4. Angular distributions of sputtered W particles under Ar irradiation, approximated with (1). Dashed lines – approximation of experimentally obtained distributions from [19]. Solid line – approximation of PARCAS code MD simulations [20].

experiment [22] that under Ar^+ ions bombardment with different (though low: 50–200 eV) energies, angular distribution of sputtered W atoms changes its shape with E_{in}. A decrease of particles incident energies leads to more shallow distribution of sputtered particles. Experimental angular distributions from [22] were approximated with (2):

$$\begin{cases} f(\theta) = 1.14\cos^{0.20}(\theta) - 1.05\cos^{0.90}(\theta)) \,|U_b = 50\text{V} \\ f(\theta) = 0.34\cos^{1.05}(\theta) - 0.29\cos^{2.05}(\theta)) \,|U_b = 100\text{V} \\ f(\theta) = 0.41\cos^{1.90}(\theta) - 0.34\cos^{3.20}(\theta)) \,|U_b = 150\text{V} \end{cases} \quad (3)$$

MD calculations using the PARCAS code [23,34–36] were also performed for Ar ions impinging on W. The MD simulations used several different W interatomic potentials, with different functional form and physical motivation [24]. They all gave very similar angular distributions, giving good confidence that the angular distribution is reliably predicted. The MD results could be also approximated with (2):

$$f(\theta) = 0.30\cos^{1.80}(\theta) - 0.45\cos^{4.00}(\theta) \quad (4)$$

All approximated distributions are shown in Fig. 4 and turn up to have quite similar shapes.

It was shown in our previous work [10] that the angular distribution of sputtered particles determines the decay rate of WI intensity along the z axis to a large extent, because geometrical losses of W escaping the plasma column dominate over ionization as the loss term. Preliminary calculations with angular distribution dependent on the E_{in} as in [22] have shown that the axial intensity profile changes its shape (to non-linear in logarithmic scale) with U_b (E_{in}) alterations, which was not the case during the PSI-2 experiments (see Fig. 3). Small decay length alterations with U_b in Fig. 3 are connected with energy distribution alteration with E_{in} (see Section 4.2). This is an interesting issue for further investigation, however for this modelling we decided to use just the MD-based formula (4) for all impact energies because it has shown the best agreement with the experiment.

4.2. Energy distribution of sputtered particles

The Thompson-Sigmund energy distribution is used for sputtered particles in ERO [25]:

$$f_E(E) = \frac{\alpha(\alpha-1)EE_b^{\alpha-1}}{(E+E_b)^{\alpha+1}} \quad (5)$$

where α – is the parameter of the distributions and E_b is the surface binding energy of the sputtered material ($E_b = 11.4$ eV for W [26]). It is known from the literature [27] that for low energies

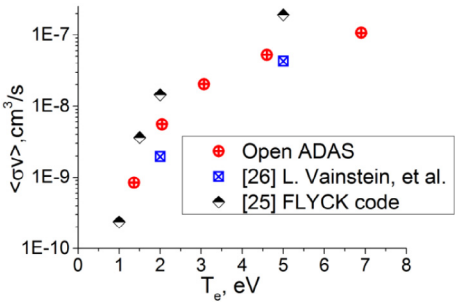

Fig. 5. Ionization data from various information sources.

of incident ions the peak of the distribution narrows and moves closer to zero. It was discussed in our previous work [10] that this effect can be represented by variation of the parameter α. Thus, for different U_b applied to the target, the distribution of sputtered particles can be approximated with the Thompson distribution using corresponding parameter $\alpha > 2$ matched to reproduce the axial decay of the WI line intensity far from the target.

We used the value $E_b = 11.4$ eV [26] in all ERO calculations, which we believe to be the most accurate. However, all SDTrimSP calculations are conducted assuming $E_b = 8.68$ eV (corresponding just to evaporation energy). This has negligible influence on ERO results because it affects only the most probable initial energy of sputtered particles: $E_{initial} = E_b/\alpha$; in our case $\alpha = 5$–15 and $E_b \approx 11.4$ eV. Thus, the most probable initial energy is always between 0.75 and 2.5 eV in our case, which has little influence on the angular distribution. Energy distribution sensitivity scan is presented in [10].

4.3. Ionization/recombination coefficients

Existing data for excitation, photon emission, ionization, recombination rate coefficients and underlying cross-sections for WI and WII from the literature and databases are quite scattered [28,29,30] (see Fig. 5). Obviously these values, ionization in particular, play a crucial role for the simulation of the neutral tungsten radiation intensity$I_{WI}(z)$ plume in front of the target surface eroded by plasma. The ionization can have strong influence on the local transport of eroded particles including prompt effects just after the surface release. For W with large mass and respective Larmor radius and, from the other side, weak electron binding, it cannot be neglected *a priori* without proper investigation. In the present work ADAS [31] ionization/recombination coefficients [30,32] were used in the ERO simulations.

In [10] it was shown that in the case that all sputtered particles start perpendicularly to the target surface the intensity profile slope near the target depends linearly on the ionization rate. This relation is not so obvious in our case due to an angular distribution of sputtered particles; however the effect of ionization is similar. It is also important to note that on our temperature interval $T_e = 2$–4 eV the respective ionization rate changes by a factor of 10, which brings an additional uncertainty to the final result. However, on the $T_e = 4$–10 eV interval corresponding to the Ne plasma it changes just by a factor of 2–3, which reduces this uncertainty in Ne experiments.

Recombination effect is similar to ionization, however, according to ADAS data, recombination rates are at least by an order of magnitude smaller than the ionization ones for considered plasma parameters, which makes their influence negligible.

4.4. Metastability effect in WI

All experimentally obtained WI spectroscopy line intensity profiles along the installation axis have a rapid growth in a near-surface target region (up to ≈ 5 mm) before the characteristic recession connected with WI ionization starts, which results in a maximum at $z \approx 5$ mm from the target surface.

The most probable explanation for this shape is that the internal state of the sputtered particles needs a certain time for excitation and eventual relaxation in the surrounding plasma. The neutral W has an unknown initial population just after the sputtering event. It can have a significantly larger emissivity for the WI $\lambda = 400.9$ nm line then it comes to the equilibrium population of its energy levels, which are determined mostly by the plasma temperature. The density can also have an influence on these populations and even more on the relaxation time. It is well imaginable that the intensity of the considered septet line can be weaker close to the target for instance due to the strong population of the quintet system just after sputtering (it should be mentioned that WI has a septet ground state).

Due to the complexity of the W ion the atomic data availability is quite poor, not mentioning the fine effects like MS populations. First attempts of such calculations are ongoing in ADAS. Still, the general effect is not new. The MS state tracking allowing considering the population relaxation between different spin systems has already been implemented into ERO for BeI [33]. As a very first approach aimed in the effect demonstration and feasibility check we can use the rates fitted from the experiment. Assuming that ionization rates from both ground and MS states are equal to the unresolved by MS values we need just to match the excitation/deexcitation rate, i.e. the system relaxation time, found to be $t_{relax} \approx 1.5 \times 10^{-5}$ s, from the WI axial profile maximum position (see Section 4.5).

4.5. Simulation results

Mass loss experiments were simulated in ERO for two available conditions (Table 1) and compared with the measurements

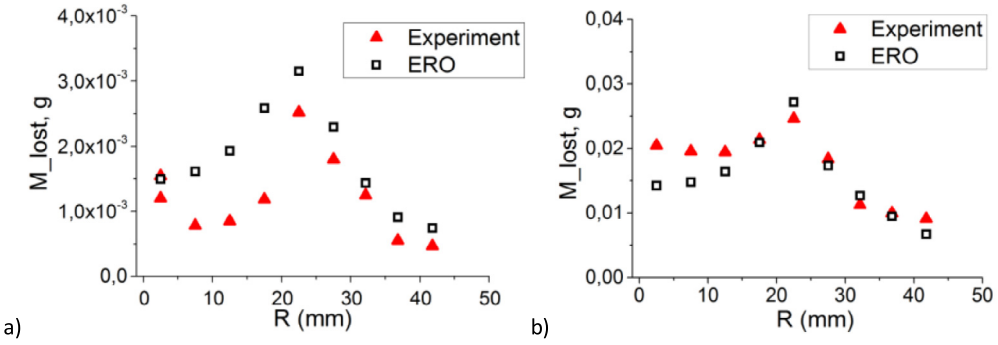

Fig. 6. Weight loss values obtained from the Ar experiment and with the ERO simulations. a) "Low" discharge power case, $U_b = 150$ V, experiment 3 (see Table 1); b) "High" discharge power case, $U_b = 150$ V, experiment 2 (see Table 1).

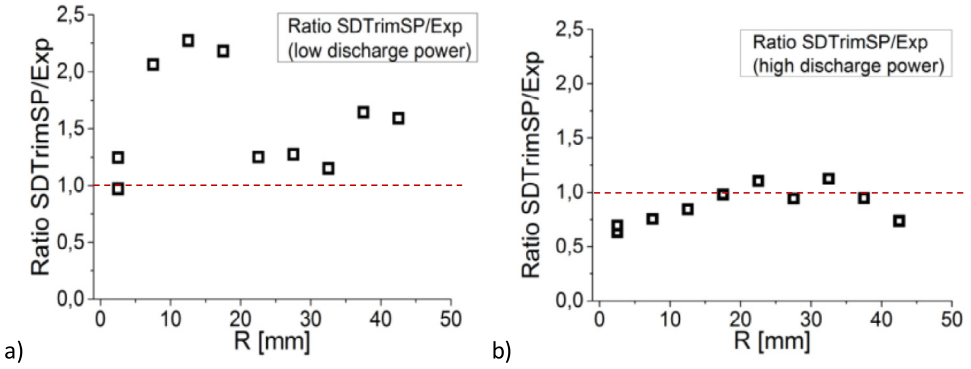

Fig. 7. Ratio between SDTrimSp-calculated and experimentally obtained sputtering yields for Ar -> W experiments radial distribution. The redeposition of the impurities is counted out from the experimental yield based on the ERO calculations. a) "Low" discharge power case, $U_b = 150$ V, experiment 3 (see Table 1); b) "High" discharge power case, $U_b = 150$ V, experiment 2 (see Table 1).

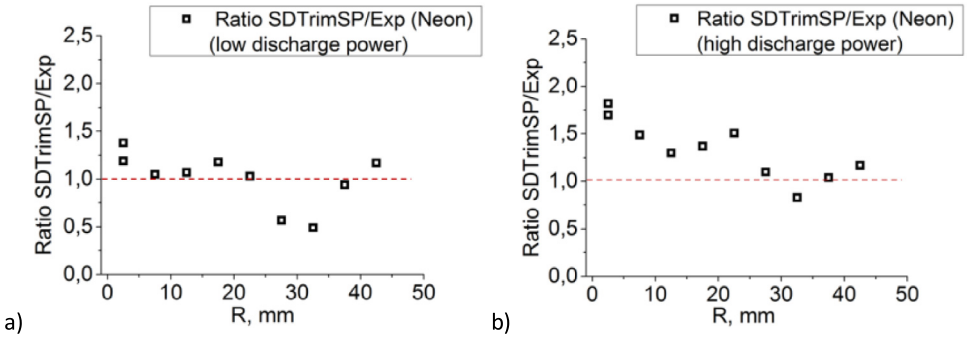

Fig. 8. Ratio between SDTrimSp-calculated and experimentally obtained sputtering yields for Ne -> W experiments radial distribution. a) "Low" discharge power case, $U_b = 165$ V, experiment 4 (see Table 1); b) "High" discharge power case, $U_b = 165$ V, experiment 4 (see Table 1).

(Fig. 6). The simulation results are in a good qualitative agreement with the experiment – the spatial distribution mimics maximum plasma density and flux position. The radial distribution of the ratio of SDTrimSP sputtering yields to the experimental ones is presented in Fig. 7. They are in a quantitative agreement within 50% for the "high" discharge power; for the "low" power case, however, there is a deviation by the factor 1.0–2.3.

These discrepancies are most probably associated with the alterations of the Ar ion flux on the way from the Langmuir probe to the target due to an intensive plasma recombination on this interval. In the ERO calculations we have already taken into account overall flux decrease by a factor of 1.5–2.1 dependent on the discharge power. The shape of the flux radial profile also changes and can be quite difficult to predict without specific measurements. Finally, the deviations can be caused by a relatively large uncertainties in the T_e measurements ($T_e = 2$–4 eV, $\Delta T_e \approx 1.5$ eV).

The recombination effects are much less prominent in the recent PSI-2 experiments on W irradiation with neon (Ne) plasmas. The mass loss measurements show a good quantitative agreement with the SDTrimSP predicted yields at least within 50% (see Fig. 8). Uncertainties in the T_e measurements and recombination do not play such crucial role here; however we cannot exclude them completely. The influence of Ne^{2+} ions is much less pronounced due to the considerably higher ionization energy of Ne^{+} (≈ 40 eV) in comparison to Ar^{+} (≈ 27 eV).

For the Ar experiments one should also note a strong redeposition of sputtered W mainly caused by the friction force experienced by the charged particle inside the plasma flowing towards the target [14]. This effect was not measured in the experiment; however it was estimated using ERO calculations. ERO shows 25% of redeposited material for the "low" discharge power and 50% of it for the "high" power case. In Figs. 6 and 7 this effect is already taken into account. Prompt redeposition contribution according to ERO estimations was negligible in our case and made up only 3–5% of the redeposited material.

Finally, it is important to note that all rates for elementary processes in ERO (ionization, recombination, etc.) are obtained with the assumption of the Maxwellian electron velocity distribution in plasma, which is most probably not the case for the PSI-2 facility due to features of plasma production in the source [18]. The detailed analysis of importance of this effect, which probably demands dedicated experiments at PSI-2 is out of the scope of the present paper.

Experimental 2D side-view emission intensity patterns composed of 14 radial intensity profiles taken at every 5 mm from the target surface were reproduced in the ERO code for 'low' and 'high' discharge power cases (see Fig. 9). ERO reproduces well the 2D distribution of the emission intensity (side view) and its alterations with the plasma parameters. However, the intensity peak at 5 mm from the target surface in the modelling (Fig. 9, right) is not resolved in experimental 2D emission patterns due to their low resolution in axial direction. Therefore, we used high-resolution axial intensity profiles (Fig. 10) for this effect analysis and corresponding ERO benchmarking.

Quantitatively the simulation results are in agreement with the experiment for the "low" discharge power and differ by a factor of 5.8 for the "high" power case. Photon emission coefficients (PECs) used for intensity calculations in ERO are very sensitive for T_e, as well as for the electron velocity distribution. Therefore, the final result of quantitative intensity is a complex interplay of the input atomic and ionization data combined with the uncertain flux alterations between the discharge power cases. Thus, one can expect a large uncertainty here, which can be diminished by choosing more optimal experimental parameters (e.g. higher T_e) and using improved PECs expected as a result of ongoing ADAS activity.

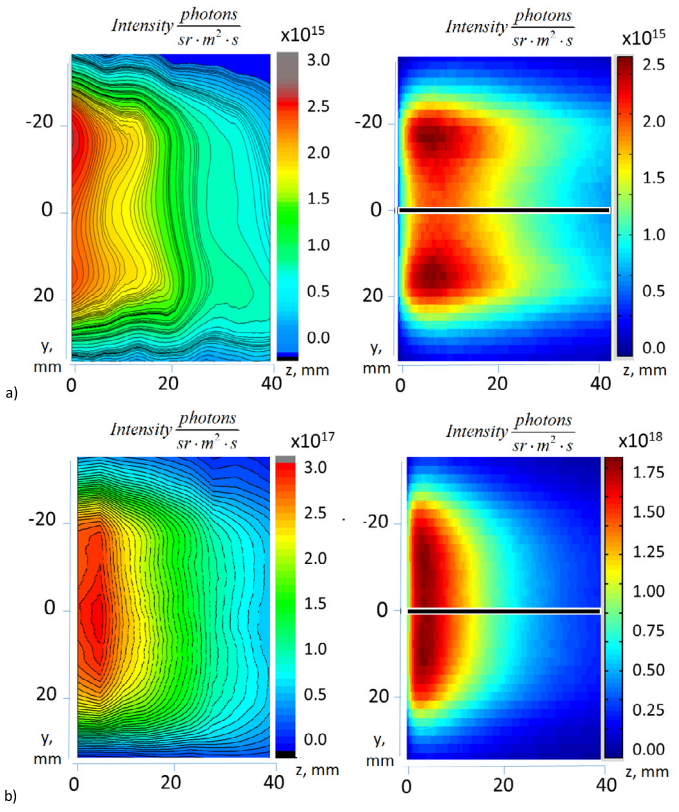

Fig. 9. 2D emission intensity patterns (λ = 4009 A) obtained in the Ar experiment with the spectrometer (left) and calculated with ERO (right). Black line – direction of axial intensity profiles extraction. a) "Low" discharge power case, $U_b = 150$ V, experiment 3 (see Table 1); b) "High" discharge power case, $U_b = 150$ V, experiment 2 (see Table 1).

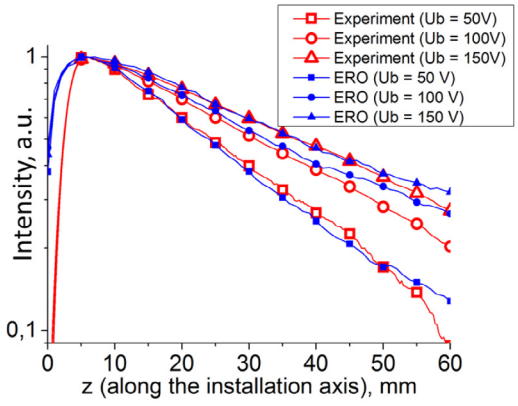

Fig. 10. Axial WI (λ = 400.9 nm) intensity profiles (normalized) – Ar experiment and ERO simulations. "Low" discharge power, $U_b = 50$–150 V, experiment 1 (see Table 1).

Emission intensity profiles along the installation axis integrated along the line of sight cross the plasma can be synthesized by ERO. Direction of profile extraction is marked with a black line in the Fig. 10, right. In the experiment these profiles were registered for every set of U_b and discharge power value. We account the intensity maximum near the target surface for the presence of WI metastable energy levels (see Section 4.4) the characteristic relaxation time t_{relax} of those determines its position. Sensitivity study using ERO have shown nearly linear dependence of the maximum position on the relaxation time t_{relax}; it was confirmed by analytical estimations of levels population with assumption of a system with one ground, one long-living excited and one ionized states. Fig. 10 demonstrates a reasonable agreement of the simulated and measured line intensity profiles.

QMB signal dependence (see Fig. 11) on the QMB-target axial distance $R_{QMB}(L)$(Fig. 1) has a quite predictable form: the QMB signal comes to zero for both very large and very small distances and has a maximum (at L ≈ 10 cm) determined most probably by the angular distribution of sputtered species, which was shown to have a "butterfly" shape (see Section 4.1). Rapid decrease of $R_{QMB}(L)$ at small distances represents the obvious geometrical influence: due to a radially shifted QMB sensor position only particles starting with a very large angle to the normal to the target surface are capable of reaching the sensor. The shape of the signal recession for larger distances represents the ionization influence: ions can reach QMB quite seldom because of trapping in the magnetic field co-directional with the installation axis. This effect however is minimal for the presented in Fig. 11 'low' discharge power case since plasma density is too low for significant ionization. For this specific case experimental results are in a good agreement with the analytical estimations based on exclusively geometry factors:

$$R_{QMB}(z) = \int_{-a/2}^{a/2}\int_{-b/2}^{b/2} \frac{S_{\perp QMB}(x,y,z)}{2\pi\left((x-x_{QMB})^2+(y-y_{QMB})^2+z_{QMB}{}^2\right)} Y \cdot F(x,y)\cdot dx\cdot dy$$

$$S_{\perp QMB}(x,y,z) = \pi r_{QMB}{}^2 \frac{z_{QMB}}{\sqrt{(x-x_{QMB})^2+(y-y_{QMB})^2+z_{QMB}{}^2}}, \quad (6)$$

where x_{QMB}, y_{QMB}, z_{QMB} – sensor position, a, b – sides of the rectangular target ((0;0;0) is at the centre of it), Y – sputtering yield and *F(x,y)* - plasma flux in a certain target point, $S_{\perp QMB}$ is the area of the QMB's circle contour projection on the plane perpendicular to the line connecting a particular point on the target surface and the sensor. The number of particles reaching the QMB sensor was estimated assuming uniform angular distribution of sputtered particles: in this case it is proportional to the solid angle calculated as $S_{\perp QMB}$ divided by the distance from the target. ERO simulation results are in a good qualitative and quantitative, within 50%, agreement with the experiment and estimations mentioned (Fig. 11).

The ERO simulations also perfectly reproduce the qualitative dependence of the QMB signal on target biasing mimicking the W sputtering yields dependence on the ion impact energy E_{in} (see Fig. 12). To reproduce the quantitative results during the scans at various discharge powers one should take into account the respective Ar^{2+} to Ar^{+} ions concentrations. Their indicative values are

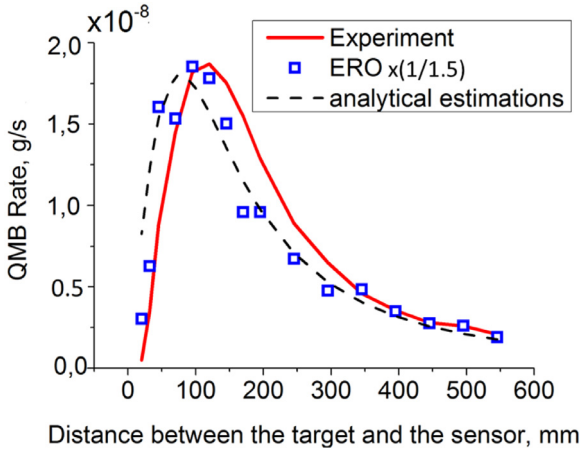

Fig. 11. QMB rate as a function of the distance between the sensor and the target (Ar experiment (experiment 3, see Table 1), ERO simulation, analytical estimations based on geometry factors only).

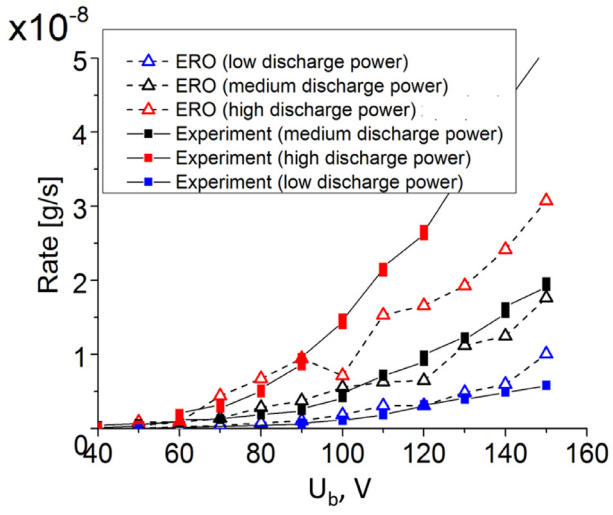

Fig. 12. QMB rate as a function of bias voltage applied to the target (U_b) and discharge power (Ar experiment (experiment 1, see Table 1) and ERO simulations).

specified in Section 2, Table 2. For the "high" discharge case, however, ERO underestimates the QMB sensor deposition rate, most probably due to the discussed uncertainties in T_e, ion flux, electron velocity distribution and ionization rates which affect strongly the species transport. These issues are likely to be minimized in the planned simulations of the experiments where Ne was used instead of Ar for W sputtering.

5. Conclusions

Recently conducted experiments on the W erosion and transport at PSI-2 were accompanied by the simulations by the 3D Monte-Carlo ERO code. Some modifications of the ERO physical model were performed for this modelling including the energy and angular distributions, WI metastables and Ar^+/Ar^{2+} ion fraction accounting. These simulations help to interpret experimental results by taking into account the interplay of various processes and finally validating the sputtering yields which can be used for the predictions for ITER and other devices.

The ERO simulations reproduce well all experimentally observed trends including the good agreement of absolute values: the weight loss at various plasma conditions in Ar and Ne plasma, the target biasing, i.e. ion impact energy, influence on the deposition of eroded particles at the QMB witness plate, 2D spectroscopic views of the W emission plume close to the target etc.

The influence of several physical effects and related uncertainties were studied. The angular distribution of sputtered W atoms was determined by comparison of the modelled deposition on the QMB with the according experimental data and confirmed by the molecular dynamics calculations. An important role of W redeposition for weight loss measurements was shown with the ERO simulations. There is up to 50% of redeposited material according to ERO. It was demonstrated that WI metastable states can explain the WI intensity profiles shape with a maximum at a distance of ≈ 5 mm from the target.

In general, our resulting sputtering yields are consistent with the SDTrimSP simulations. The quantitative agreement is within 50% for all considered benchmark ERO applications but spectroscopy. Remaining discrepancies are associated with uncertainties in the atomic data, possible deviations of electron velocities in the PSI-2 plasma from the Maxwellian distribution, flux variations on the way from the Langmuir probe to the target due to recombination and uncertainties in T_e measurements. Further experiments for instance with higher T_e are necessary to eliminate the remaining uncertainties.

Acknowledgements

The authors are deeply thankful to I. Sorokin for providing the data on Ar^{2+} concentration in the plasma of the PSI-2 facility. The work is carried out in the frame of FZJ-MEPhI strategic partnership.

References

[1] V. Philipps, J. Nucl. Mater. 415 (1) (2011) S2–S9.
[2] R.P. Doerner, et al., Phys. Scr. T111 (2004) 75.
[3] G.J. van Rooij, et al., Appl. Phys. Lett. 90 (2007) 121501.
[4] A. Kreter, et al., Fusion Sci. Technol. 68 (1) (2015) 8–14.
[5] A. Pospieszczyk, et al., J. Nucl. Mater. 438 (2013) S1249–S1252.
[6] A. Kreter, Fusion Sci. Technol. 59 (1) (2011) 51–56 T.
[7] A. Kirschner, et al., J. Nucl. Mater. 363-365 (2007) 91–95.
[8] D. Borodin, et al., J. Nucl. Mater. 390–391 (2009) 390–391.
[9] D. Borodin, et al., Contrib. Plasma Phys. 50 (3-5) (2010) 432–438.
[10] E. Marenkov, et al., J. Nucl. Mater. 463 (August) (2015) 268–271.
[11] W. Eckstein, Topics in Applied Physics 110 (2007) 33–187.
[12] A. Kreter, et al. 22nd International Conference on Plasma-Surface Interactions in Controlled Fusion Devices (2016).
[13] I. Sorokin, et al. 22nd International Conference on Plasma-Surface Interactions in Controlled Fusion Devices (2016).
[14] A. Kirschner, et al., Nucl. Fusion 40 (2000) 989.
[15] C. Birdsall. Plasma Physics Via Computer Simulation, McGraw-Hill, Singapore 1985.
[16] H.P. Summers, The ADAS User Manual, 2004 version 2.6 http://adas.phys.strath.ac.uk.
[17] P.C. Stangeby, Phys. Fluids 27 (11) (1984) 1958–1988.
[18] B. LaBombard, et al., J. Nucl. Mater. (1989).
[19] D.G. Whyte, et al., Nucl. Fusion 41 (1) (2001).
[20] G. Betz, et al., Int. J. Mass Spectrom. Ion Processes 140 (1) (1994) 1–110.
[21] Y.V. Martynenko, et al., Tech. Phys. 57 (4) (2012) 439–444.
[22] D. Nishijima, et al., J. Nucl. Mater. 415 (1) (2011) S96–S99.
[23] K. Nordlund, 2006, PARCAS computer code. The main principles of the molecular dynamics algorithms are presented in [35, 36]. The adaptive time step and electronic stopping algorithms are the same as in [34].
[24] A.E. Sand, et al., J. Nucl. Mater. 455 (2014) 207–211.
[25] A. Goehlich, et al., J. Nucl. Mater. 266-269 (1999) 501–506.
[26] X. Yang, et al., Appl. Surf. Sci. 293 (2014) 187–190.
[27] R. Brizzolara, et al., Nucl. Instrum. Methods Phys. Res. B35 (1988) 36–42.
[28] H.K. Chung, et al., High Energy Density Phys. 1 (1) (2005) 3–12.
[29] L. Vainshtein, et al., Ionization of W atoms and W+ ions by electrons, Journal of Physics B: Atomic, Molecular and Optical Physics 44 (12) (2011) 125201.
[30] S.D. Loch, et al., Phys. Rev. A 72 (5) (2005) 052716.
[31] H.P. Summers, et al. In Atomic and Molecular Data and Their Applications (AIP Conference Proceedings Series Volume 901) (vol. 901, pp. 239–248).
[32] T. Pütterich, et al., Plasma Phys. Controlled Fusion 50 (8) (2008) 085016.
[33] D. Borodin, 36th EPS Conference on Plasma Physics, vol. 33E, ECA, 2009 P-5.197 (2009).
[34] K. Nordlund, Comput. Mater. Sci. 3 (1995).
[35] C.S. Madi, et al., J. Phys. Condens. Matter 21 (2009) 224010.
[36] K. Nordlund, et al., Phys. Rev. B 57 (1998) 7556.
[37] D. Borodin, et al. Proceedings of 22nd International Conference on Plasma-Surface Interactions in Controlled Fusion Devices (2016). Submitted to NME.